ICARUS **127,** 173–189 (1997)
ARTICLE NO. IS975687

Titan's North–South Asymmetry from HST and Voyager Imaging: Comparison with Models and Ground-Based Photometry

RALPH D. LORENZ, PETER H. SMITH, MARK T. LEMMON, AND ERICH KARKOSCHKA

Lunar and Planetary Laboratory, Department of Planetary Sciences, University of Arizona, Tucson, Arizona 85721–0092
E-mail: rlorenz@lpl.arizona.edu

G. W. LOCKWOOD

Lowell Observatory, 1400 W. Mars Hill Road, Flagstaff, Arizona 68001

AND

JOHN CALDWELL

Department of Physics and Astronomy, York University, 4700 Keele Street, North York, Ontario, Canada M3J 1P3

Received February 20, 1996; revised December 2, 1996

New measurements of Titan's hemispheric brightness asymmetry from HST images from 260 to 1040 nm show that the contrast is strongest near 450 nm (blue) and, with the opposite sign, at 889 nm (methane band). Comparison with a full Titan year of disk-integrated albedo data indicates that the seasonal cycle in asymmetry is smooth, but is insufficient to explain the variation in albedo, and a twice-per-year global albedo enhancement 50% larger than the hemispheric asymmetry amplitude is required, as noted by other workers. We also report measurements of limb-darkening (strongest at red wavelengths) and note that the transition zone between the "hemispheres" lies in the northern, brighter hemisphere at present. Comparison of models to the HST data set indicates that a change in aerosol number density above 70 km, and largely below 120 km, is the likely mechanism and is probably driven by aerosol transport by meridonal and vertical winds. © 1997 Academic Press

1. INTRODUCTION

Titan was little more than an unresolved dot in the sky until the Pioneer 11 and Voyager 1 and 2 encounters in 1979, 1980, and 1981. Its appearance in the Voyager images was disappointingly bland, since the surface was hidden by a thick atmosphere laden with an opaque haze (Smith *et al.* 1981). The dominant feature in the many images was a distinct variation in brightness from north to south, termed the north–south asymmetry (hereafter NSA). The NSA was investigated in some depth by Sromovsky *et al.* (1981), who compared Voyager 1 (V1) measurements with those of Pioneer 11 some months before, and reported by Tomasko and Smith (1982). Examination of the Voyager 2 (V2) data in Smith *et al.* (1982) reported no significant variation from V1 to V2, consistent with a seasonally varying asymmetry at a peak in the early 1980s (i.e., near equinox). Such a seasonally controlled asymmetry would be expected to reverse in sign within a decade.

Caldwell *et al.* (1992) observed Titan in 1990 using HST and the Wide Field/Planetary Camera (before the replacement by WFPC2). They measured the NSA in two filters (blue and green) and noted that the NSA had reversed compared with Voyager, with the northern hemisphere now brighter than the south. They also noted, although with a poor signal-to-noise ratio, that an image in the 889-nm methane band had a NSA opposite in sense from that seen at visible wavelengths. Such a wavelength dependence is consistent with the modeling of Toon *et al.* (1992) who noted that an increased haze optical depth reduces the albedo at short wavelengths (below 600 nm) but increases albedo at longer wavelengths.

We here report analyses of subsequent HST images to provide a fuller data set for future modeling efforts and compare the asymmetry with that measured in Voyager data. The seasonal variation in the asymmetry has been suggested as the explanation for the variation in Titan's disk-integrated albedo, although previous investigations (e.g., Sromovsky *et al.* 1981, 1986, Lockwood *et al.* 1986) have noted that the asymmetry observed by Voyager is inadequate to completely describe the albedo variation.

Additionally, we examine albedo variations produced in a number of models, to constrain the likely mechanism and point out directions for future modeling efforts.

0019-1035/97 $25.00

TABLE I
HST Images of Titan Used or Referred to in this Study

Proposal ID	Archive #	Instrument	Date	Filter	Exposure (s)	Distance (AU)	Comments
2891							PI Westphal Phase=4.0°, Sub-Earth Latitude=24.0° Sub-Solar Latitude=23.0°
	WOCL0101T	WF/PC-1	26 Aug 1990	F439W	2	9.245	Cosmic Ray Blemish - see Caldwell et al (1992)
	WOCL0102T	WF/PC-1	26 Aug 1990	FQCH4N-D	14	"	Badly underexposed
	WOCL0103T	WF/PC-1	26 Aug 1990	F547M	1	"	
1289							PI Caldwell Phase=5.4°, Sub-Earth Latitude=15.1° Sub-Solar Latitde=16.6
	X0Z40201T	FOC	26 Jun 1992	F231W+F231M	1507	9.138	Very Noisy
3899							PI Smith Phase=1.4°, Sub-Earth Latitude=16.7° Sub-Solar Latitude=16.1°
	W1130101T	WF/PC-1	21 Aug 1992	F336W	500	8.908	
	W1130102T	WF/PC-1	21 Aug 1992	F588N	100	"	
	W1130103T	WF/PC-1	21 Aug 1992	F547M	10	"	
	W1130104T	WF/PC-1	21 Aug 1992	F439W	50	"	
	W1130105T	WF/PC-1	21 Aug 1992	FQCH4N-D	500	"	
	W1130106T	WF/PC-1	21 Aug 1992	F791W	4	"	
	W1130107T	WF/PC-1	21 Aug 1992	F850LP	7	"	
	W1130108T	WF/PC-1	21 Aug 1992	F673N	60	"	
5508							PI Smith Phase=3.3°, Sub-Earth Latitude=7.7° Sub-Solar Latitude=6.0°
	U2IZ0101T	WFPC2	4 Oct 1994	F336W	160	8.862	
	U2IZ0102T	WFPC2	4 Oct 1994	F439W	40	"	
	U2IZ0103T	WFPC2	4 Oct 1994	F547M	7	"	
	U2IZ0104T	WFPC2	4 Oct 1994	F588N	40	"	
	U2IZ0105T	WFPC2	4 Oct 1994	F673N	40	"	Several images exist (see Smith et al., 1996)
	U2IZ0106T	WFPC2	4 Oct 1994	F791W	3	"	
	U2IZ0107T	WFPC2	4 Oct 1994	F850LP	22	"	Several images exist (see Smith et al., 1996)
	U2IZ0108T	WFPC2	4 Oct 1994	FQCH4N-D	100	"	Several images exist (see Smith et al., 1996)
	U2IZ0109T	WFPC2	4 Oct 1994	FQCH4N-B	80	"	Several images exist (see Smith et al., 1996)
	U2IZ010AT	WFPC2	4 Oct 1994	F1042M	200	"	Several images exist (see Smith et al., 1996)

Note. Where many (>2) images in the same filter exist, only one has been listed here.

2. HST OBSERVATIONS

The available images of Titan are summarized in Table I, together with the parameters required to reduce the data. The initial observations by Caldwell (proposal ID 1289) suffered from poorly exposed images as HST's capability to track solar system objects had not yet been implemented. Also, the details of the image depended on which deconvolution process was applied to correct for the spherical aberration in the primary mirror.

A more extensive data set was obtained in 1992 by Smith (proposal ID 3899), again using WF/PC-1. This time, measurements had much better signal-to-noise, as the HST tracking capability now enabled longer exposures.

The vastly improved capabilities of WFPC2 enable us to study Titan images directly, without needing to implement image deconvolution. Smith (proposal ID 5508) obtained a series of images in October 1994. Most of these used the F850LP filter, which probes to Titan's surface, to build up a map of relative surface albedo (Smith *et al.* 1996) but additionally a suite of visible filters was used to measure the NSA. A subsequent set of images was obtained the following year (proposal ID 6295).

A set of images of Saturn and Titan spanning visible, UV, and near-infrared images were obtained by Tomasko and Karkoschka (proposal ID 6030). Most images are on the Planetary Camera, as with the previous data sets, although two use one of the wide-field cameras (giving higher signal-to-noise, at the expense of spatial resolution: Titan is about 10 pixels across, as against about 19 on the PC). Use of this data set requires caution, in that HST was tracking Saturn, not Titan, so Titan's orbital motion around Saturn produces some smearing, especially for the long exposures. However, this smearing is not catastrophic except for the very long 889-nm exposure (since the direction of smearing is orthogonal to the NSA and so affects both hemispheres the same way). These images also show Titan's shadow on Saturn, which has been analyzed in a separate paper (Karkoschka and Lorenz 1997).

2.1. Data Reduction

Conventional flatfielding and dark subtraction was performed during HST pipeline processing. We made no attempt to make absolute radiometric calibration of our images, as we are examining only relative brightness. Almost

TABLE I—*Continued*

Proposal ID	Archive #	Instrument	Date	Filter	Exposure (s)	Distance (AU)	Comments
6030							PI Tomasko Phase=3.9°, Sub-Earth Latitude=-0.1° Sub-Solar Latitude=1.5°
	U2QE0201T	WFPC2 (WF4)	6 Aug 1995	F255W	300	8.820	
	U2QE0202T	WFPC2 (WF4)	6 Aug 1995	FQCH4N-C	12	"	
	U2QE0203T	WFPC2	6 Aug 1995	F336W	70	"	
	U2QE0204T	WFPC2	6 Aug 1995	F467M	16	"	
	U2QE0205T	WFPC2	6 Aug 1995	FQCH4N-B	30	"	
	U2QE0206T	WFPC2	6 Aug 1995	F673N	18	"	
	U2QE0207T	WFPC2	6 Aug 1995	F953N	100	"	
	U2QE0208T	WFPC2	6 Aug 1995	FQCH4N-D	500	"	
6295							PI Caldwell Phase=1.6° (29/9)-2.4 (7/10) Sub-Earth Latitude=1.8° Sub-Solar Latitude=0.8°
	U2VI1507T	WFPC2	29 Sep 1995	F791W	3	8.639	
	U2VI1508T	WFPC2	29 Sep 1995	F791W	3	"	
	U2VI1509T	WFPC2	29 Sep 1995	F336W	160	"	
	U2VI1101T	WFPC2	1 Oct 1995	F850LP	20	8.644	Several other images exist
	U2VI1102T	WFPC2	1 Oct 1995	F673N	40	"	Several other images exist
	U2VI1103T	WFPC2	1 Oct 1995	F1042M	260	"	Several other images exist
	U2VI1209T	WFPC2	6 Oct 1995	FQCH4N-D	260	8.672	Several other images exist
	U2VI1307T	WFPC2	7 Oct 1995	F547W	7	8.679	
	U2VI1308T	WFPC2	7 Oct 1995	F439W	40	"	
	U2VI1309T	WFPC2	7 Oct 1995	F588N	40	"	
	U2VI130AT	WFPC2	7 Oct 1995	F588N	40	"	
	U2VI130BT	WFPC2	7 Oct 1995	F953N	100	"	

all of our images were obtained near the center of the WFPC2 image plane, where optical distortion by the HST planetary camera is well under 0.5%. However, we corrected the program 6030 data set for distortion, as Titan was near the edge of the camera field of view.

We have also examined a number of flatfielded and dark-subtracted Voyager images. No corrections for geometric distortion were needed or applied. The Voyager images in general have lower signal-to-noise than the HST images, but do not suffer significant degradation from the point-spread function.

Our adopted method of determining the asymmetry is related to that used by Sromovsky *et al.* (1981) although rather than scanning along a meridian we take points from all radial positions on the disk. We divide the disk into a north and a south section and ignore points with latitudes less than $\pm 20°$. For each of these sections, a least-squares (uniform weighting) linear fit to $\log(I\mu)$ against $\log(\mu\mu_0)$ was determined (see Fig. 1), where I is the observed flux (which we assumed proportional to image data number DN after dark subtraction and flatfielding), μ is the cosine of the emission angle, and μ_0 the cosine of the solar zenith angle of each point. A straight-line fit indicates that the hemisphere follows a Minnaert law of the form $I = I_0\mu^k\mu_0^{k-1}$: the slope of the line corresponds to k, which has values typically between 0.5 (uniform disk) and 1.0 (Lambertian sphere), and I_0 is the intercept of the line with $\mu\mu_0 = 1$ and is a measure of the relative albedo of the hemisphere. The north/south albedo ratio—which we will abbreviate as NSA, since the asymmetry and the albedo ratio are the same physical entity—is simply the ratio of the intercepts for the two hemispheres. Note that if k differs substantially between hemispheres, the lines could cross, giving a higher intercept value to the hemisphere with the dimmer limb. However, in practice we find that the k slopes are virtually the same between hemispheres.

Figure 1 shows plots of $I\mu$ vs $\mu\mu_0$ for two images, one blue (F439W) and one methane band (FQCH4N-D, at 889 nm). It is clear that the blue image is well-described by such a model—most of the points for each hemisphere fall on or near a straight line.

Selecting segments further from the center of the disk enables distinct separation of the two hemispheres: the near-equatorial data points depart from the two straight lines, due to the "blurring" near the interhemispheric boundary. Excluding points closer than 20° from the equator eliminates this problem. Since points further from the center of the disk (i.e., those with lower μ) are more prone to center-finding errors and, having lower signal, are noisier, we excluded pixels with $\mu\mu_0 < 0.1$ from the fits. As can be seen in Fig. 1b, this selected subset of points allows a much better fit, indeed with a correlation coefficient R for both lines greater than 0.995. Good fits of this type are found for images at wavelengths less than 700 nm.

The methane band image has a somewhat different character, with points in both hemispheres (Fig. 1c) falling near curves which are neither straight nor parallel, suggesting a Minnaert fit fails to capture the full complexity of Titan's appearance at this wavelength. Thus, the ratio of intercepts or the ratio of points with a given $\mu\mu_0$ does not fully

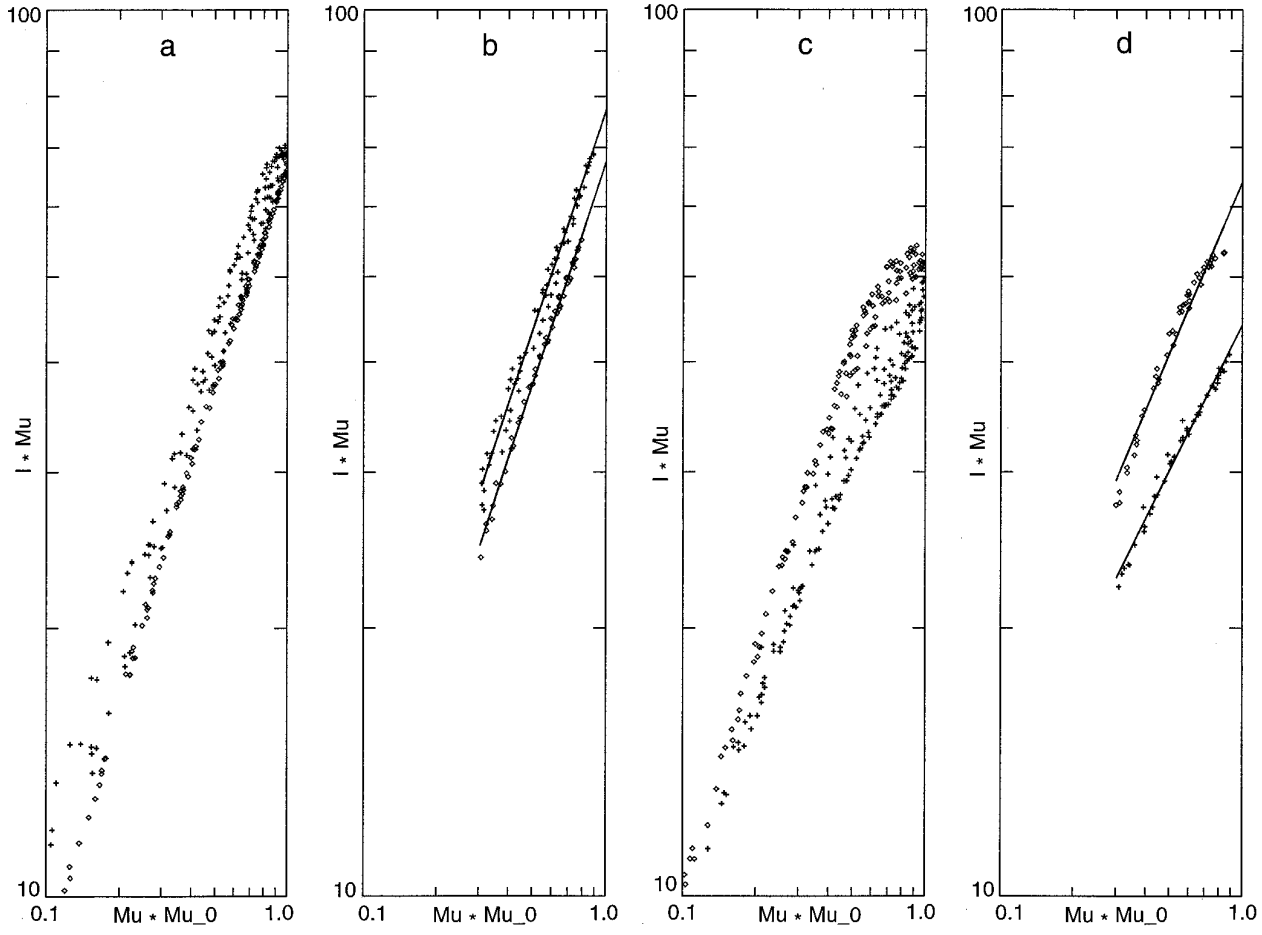

FIG. 1. Logarithmic $I\mu$ vs $\mu\mu_0$ plots for two images: a,b F467M, c,d FQCH4N-D (889 nm). Crosses are points in the northern hemisphere; diamonds are in the south. (a and c) All points with $\mu\mu_0 > 0.1$; (b and d) only points further than 20° from the equator and with $\mu\mu_0 > 0.3$, where a better fit can be made—the ratio of the fitted line intercepts is used to estimate the north/south albedo ratio. Note the substantial non-linearity of the methane band data.

describe an albedo ratio. However, in order to generate a parameter for year-to-year and model comparisons, we applied the same method as before. Although the fit (Fig. 1d) to the dimmer northern hemisphere is reasonable ($R = 0.985$), the southern hemisphere has a pronounced kink and a poorer correlation coefficient ($R = 0.95$). Although future efforts should investigate and attempt to reproduce the shape of the curves, the present paper retains a straight line fit, as this appears to provide sufficient fidelity for the current generation of models.

2.2. *Error Analysis*

Our Minnaert fits suffer from four sources of error. First, the two-albedo Minnaert function does not completely describe Titan's appearance—Fig. 2 in Sromovsky *et al.* (1981) and Fig. 15 in Smith *et al.* (1982) show their determined albedo as a function of latitude—it is not perfectly described by only two albedo values. Also, images using filters which sample the near-infrared methane bands (F791W, F850LP, F1042M, and FQCH4N-C and -D) are not well described by the Minnaert fits, as there is both limb-brightening and darkening present.

Second, the HST point-spread function (psf) causes some blurring. This causes the transition between north and south to be less distinct than it would otherwise be, and the limb profile is flatter than would be the case in a sharp image. These two errors have a modest effect on our fits, since we exclude pixels with $\mu\mu_0 < 0.1$, and we eliminate the near-equatorial band in any case. Since the core of the psf is only a couple of pixels wide, the albedo ratio estimate is not significantly affected, and both hemispheres are in any case affected in the same way.

The third source of error is noise in the data itself. For most images, the peak brightness is >500 DN, with a gain of 7 or 14 electrons/DN, so quantization noise is negligible

and poisson noise is <1% (the F255W image has a lower signal, however). The flat field errors are 1–2%, with the exception of F336W, where it is perhaps 4%. However, most of this variation is from one pixel to the next (rather than an across-image gradient) so the albedo ratio estimate does not suffer systematically.

The final, and principal, source of error, is in the μ and μ_0 values used for the points in the fit. This in turn is due to errors in the determination of the center of the disk and inaccuracy of the assumed or measured radius. We used the wavelength-dependent radius from Toon *et al.* (1992). We determined the center of the image by taking the mean of the points of maximum intensity gradient. This method suffers slightly in the presence of non-zero phase angles, but error in center-finding can be easily identified, by an asymmetric brightening at the edge of the disk when the model is subtracted from the image and corrected accordingly.

We estimate, conservatively, that the center can be determined to ~2% of the radius (about 0.2 HST pixel). Note that the determined Minnaert coefficients and albedo ratio are relatively insensitive to east–west errors in center location. By considering the μ and μ_0 values calculated for a point near the center of the disk ($\mu = 0.94$) and for a point near the edge (nominal $\mu\mu_0 = 0.3$), it can be shown by numerical experiment that for no east–west center-finding error but a center estimate 2% to the north of true, the albedo ratio will be estimated 0.03 too low, and the k values will be 0.01 too high for the north and 0.01 too low for the south. These error values are for where the true k value is 0.8 and the albedo ratio is 1.1: the errors are smaller if the true k is smaller and vice versa (e.g., if true $k = 0.6$, the corresponding errors in estimate of albedo ratio and k are 0.01 and 0.005, respectively).

To verify this accuracy estimate, we made synthetic images with specified albedo ratio and k and attempted to retrieve these parameters using the same processing we applied to the real images. Typically, we can recover the albedo ratio to within ± 0.02 and the k values to within ± 0.05 for true $k = 0.8$.

To avoid introducing deconvolution artifacts into the images, we used raw (undeconvolved) images in this study. To investigate the effect of the HST psf, we convolved synthetic images with wavelength-dependent point-spread functions generated using TinyTIM software developed by John Krist and available from STScI: we found that the recovered albedo ratios were the same (within 0.01) of those for the original images, but the fitted k values were consistently 0.05 to 0.07 higher than they should be. The effect is essentially an enhancement of limb-darkening induced by ''blurring in'' the darkness of space into the edge of the disk.

To evaluate the applicability of a three-parameter model to the real Titan, we fit albedo ratio and k values to an image and then subtract a model image created using specified center and radius (we used the wavelength-dependent radius of Toon *et al.* (1992)) and the determined Minnaert coefficients and albedo ratio. The synthetic image has a transition region (typically 20° wide) at about 10°N , where the brightness is the latitude-weighted mean of the values for the two hemispheres. For the most part, the residuals (see Fig. 2) are small—for example, the fit to the F467W image has a root-mean-squared error of 9.2 DN, or about 1.5% of peak intensity. When compared with the ~1% flatfield error and poisson noise, this suggests that the model is an accurate description of Titan's appearance. Errors are much larger and have a non-random appearance, for the near-IR images—as mentioned above, the Minnaert fit is a poor description of Titan at these wavelengths.

3. RESULTS

Our results are expressed as a north/south albedo ratio and listed in Table II and shown in Figs. 3 and 4. There is agreement between our values and those of Sromovsky *et al.* (1981) for Voyager. Within error bars, the asymmetry and limb darkening that we determine for Voyager and HST images are about the same, although the albedo ratio is perhaps slightly lower for the present than in the Voyager epoch.

The wavelength dependence of the NSA (see Fig. 3) is the same as seen in the Voyager images, with a peak at ~450 nm. Longward of 700 nm, there is a remarkable change in character of the images. The reversal in sense of the asymmetry beyond 600 nm was predicted by Toon *et al.* (1992) and noted by Caldwell *et al.* (1992) in the first HST images. Subsequent analyses were also made by Smith *et al.* (1992) and Smith and Lemmon (1993). The reversal is due to the increasing albedo of the aerosols with wavelength, such that they are darker than the bright atmosphere beneath at blue wavelengths, whereas they are brighter than the absorbing atmosphere in the infrared—particularly in methane absorption bands where the atmosphere is darkest.

It is seen that there is a reversal of the asymmetry in the 619 nm methane band, although the contrast is small. In the continuum just beyond, at 650–700 nm, the asymmetry is the same sense as at blue and green wavelengths. Beyond 700 nm, the asymmetry reverses in sense and indeed becomes stronger even than at blue wavelengths. The differing magnitude of the NSA in filters longward of 600 nm depends principally on how much methane absorption they sample, with the 889 nm methane band contributing most significantly in the F850LP and FQCH4N-D (889 nm) filters and the 1000-nm band to F953N and 1042M. Disentangling the contributions of the different

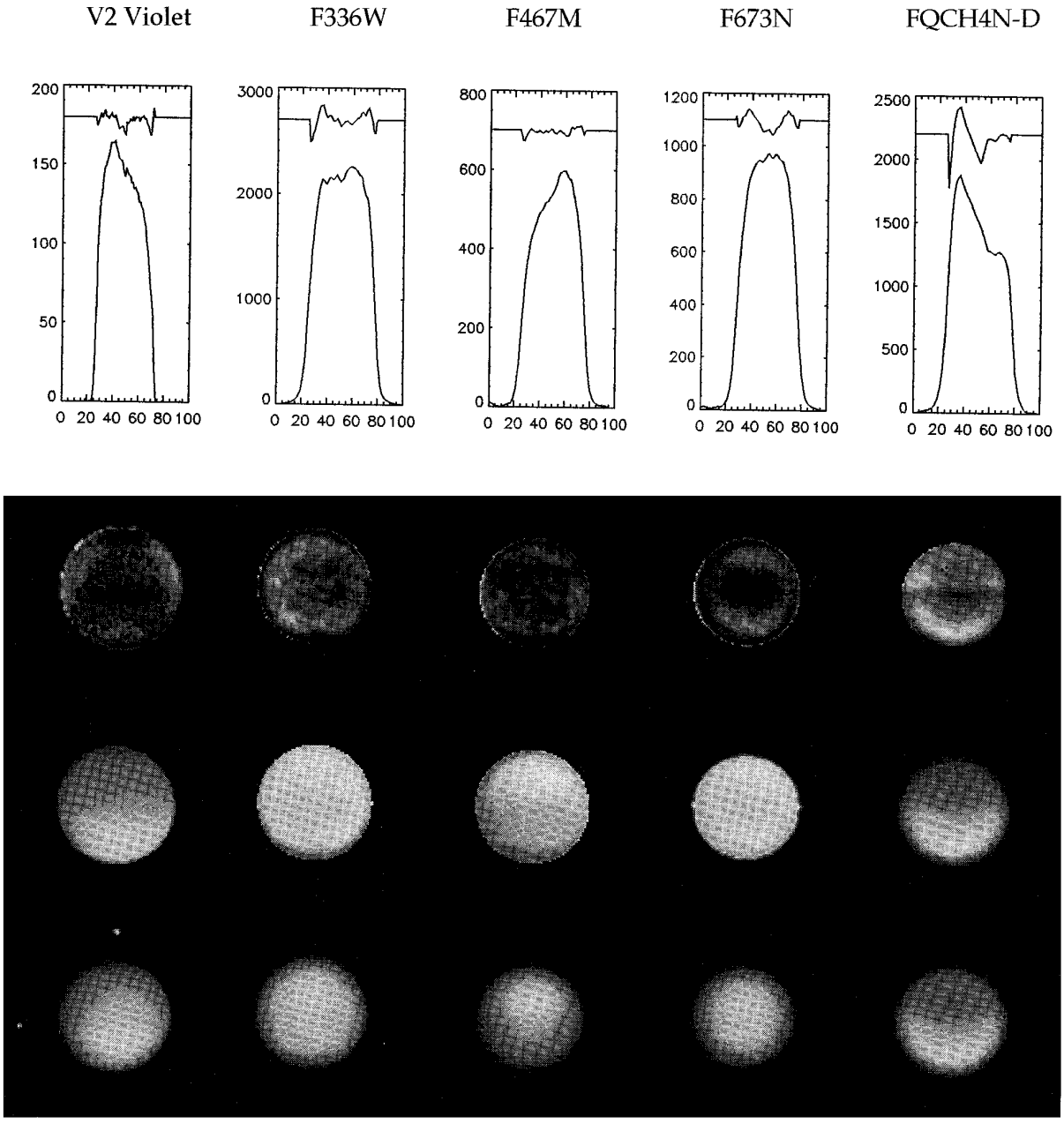

FIG. 2. Examples of flatfielded, dark-subtracted images (bottom) used in this study, left to right, Voyager 2 violet (left), HST F336W, F467M, F673N, and FQCH4N-D (889 nm). The middle-row images are "flattened," i.e., have limb darkening removed. The top row shows contrast-stretched images after subtracting a model image. Note the dark polar hood in the Voyager image. Above the images are shown north–south cuts of raw images and residuals. The curves may be used to calibrate the gray scale of the residual images. Note how well F467M is fit by model and how poorly the methane band image is fit.

bands will require detailed analysis, beyond the scope of this investigation.

The variation of brightness over the disk varies in a characteristic fashion, following a Minnaert fit as described above, except in the near-IR. Sromovsky *et al.* (1981) determined Minnaert slopes k of 0.773, 0.887, and 0.942 for violet, blue, and green V1 images, respectively. No uncertainties or differences between hemispheres were reported. Our own Voyager analysis suggests similar values of 0.75, 0.93, and 1.02, although we also estimate UV and orange Minnaert slopes of 0.65 and 1.02. When corrected for the ~0.06 offset due to the blurring by the psf, our estimates of k from visible and UV HST images are about the same as seen by Voyager (see Fig. 4). Beyond 700 nm, the Minnaert

TABLE II
North/South Albedo Ratios for Pioneer and Voyager, HST Prior to Repair and Post-Repair

Pioneer/Voyager	Mean λ	Min λ	Max λ	1979.7	1980.9	1981.7
Pioneer Blue	440	390	490	0.79±0.03[a]		
Pioneer Red	640	595	700	0.95[b]		
Voyager UV	346	325	375		0.94±0.04	0.93±0.04
Voyager Violet	416	380	450		0.80[a],0.82±0.04	0.84±0.04
Voyager Blue	479	430	520		0.80[a]	0.80[c],0.81±0.04
Voyager Green	566	530	600		0.83[a]	0.87±0.04
Voyager Orange	591	570	610			0.94±0.04
Voyager CH4_JS	618				1.03±0.04	
HST WF-PC				1990.75	1992.75	
F336W	337	305	360		1.02[f]	
F439W	431	395	465	1.14[d]	1.15[f]	
F547W	549	515	580	1.09[d,e]	1.11[f]	
F588W	589	586	593		1.06[f]	
F673N	673	670	677		1.04[f]	
FQCH4N-D	890	889	897	0.79[e]	0.7[f]	
HST WFPC-2				1994.7	1995.6	1995.8
F255W	260	235	285		1.08±0.05	
F336W	337	305	360	1.07±0.04	1.07±0.03	1.08±0.03
F439W	431	395	465	1.18±0.03		1.18
F467M	467	455	478		1.22	
F547W	549	515	580	1.18±0.03		1.15
F588N	589	586	593	1.13		1.09
F673N	673	670	677	1.02±0.03	1.03	1.03
FQCH4N-B	620	618	623	0.98	0.99	
FQCH4N-C	729	726	731		0.88±0.1	
F791W	788	788	880	0.91±0.04		0.92±0.03
F850LP	910	850	960	0.82±0.05		0.85±0.05
FQCH4N-D	890	889	897	0.78±0.05		0.78±0.05
F953N	954	951	958		0.93±0.04	0.90±0.04
F1042M	1019	990	1030	0.80±0.05		0.85±0.05

Note. Values are determined from the method described in the text, except where indicated. Where the determination is our own, the uncertainty is ±0.02 unless otherwise indicated. References are [a]Sromovsky *et al.* (1981), [b]Tomasko and Smith (1982), [c]Smith *et al.* (1982), [d]Caldwell *et al.* (1992), [e]Smith *et al.* (1992), and [f]Smith *et al.* (1994) and previously unpublished work. All wavelength ranges are in nanometers and include system response as well as filter bandpass. Mean wavelengths for Voyager are effective wavelengths under Jupiter illumination from Smith *et al.* (1977) and average wavelengths for HST are from Burrows (1995). Mean wavelengths under solar illumination are virtually the same as mean throughput wavelengths above, except for F255W, which has mean solar wavelength of 275 nm. Maximum and minimum wavelengths listed here are for ~50% of peak throughput, estimated from Fig. 6 in Smith *et al.* (1977)—see Also Danielson *et al.* (1981)—and Appendix 8.2 of Burrows (1995). Pioneer bandpass data are from Fig. 3 of Tomasko and Smith (1982).

slope falls to low values (~0.5 at 889 nm) but the Minnaert fit is poor in any case at these wavelengths. Limb brightening at long wavelengths is consistent with the scenario indicated above, with light scattered at high altitude, above a darker lower atmosphere.

Since the altitude of the limb varies with latitude by 50–100 km (see Karkoschka and Lorenz, 1997), better fits could be made with different radii for the two hemispheres. Our estimates of k for the brighter hemisphere tended to be slightly lower than for the darker, but the difference may be due to an error in assumed radius rather than a real difference in limb-darkening behavior and was smaller than our estimated uncertainty of ±0.05. We used the wavelength-dependent radius from Toon *et al.* (1992) for both hemispheres—Karkoschka and Lorenz (1997) show that these values are good global average values.

As observed by Caldwell *et al.* (1992), we find that the NSA has reversed since the Voyager epoch. We find the amplitude of the NSA relatively flat between 1992.6 and 1995.8, consistent with a peak in or near this interval. This in turn is consistent with the estimated phase lag of 85–90° of the contrast behind the solar forcing (Smith *et al.* 1981, 1982, Sromovsky *et al.* 1981). Our new data are unable to constrain the phase further, since as in the Voyager epoch,

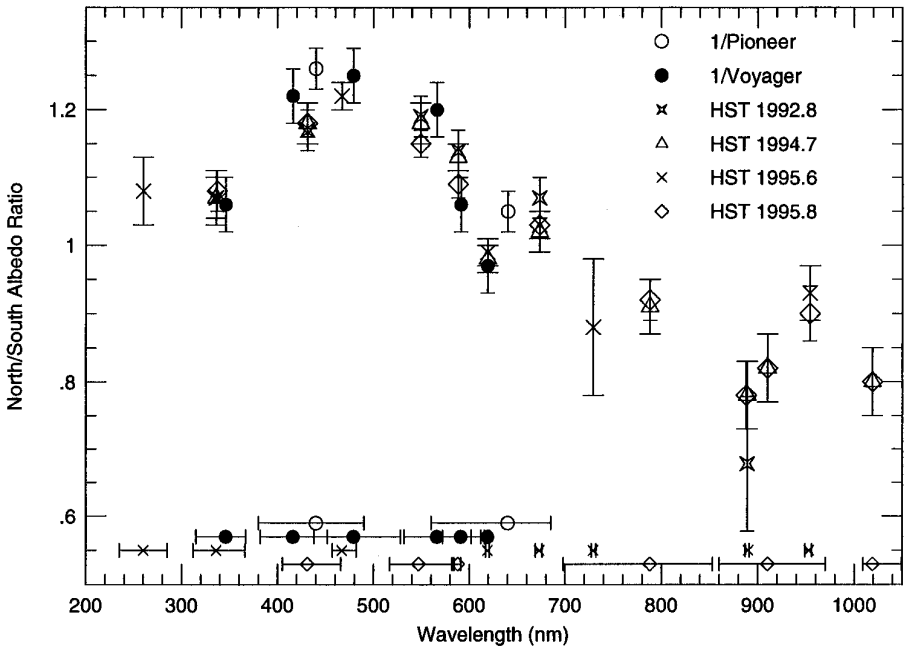

FIG. 3. Wavelength dependence of the north/south albedo ratio from HST measurements. Reciprocals of Voyager and Pioneer data are shown for comparison. Horizontal bars at bottom indicate wavelength coverage of the different filters used.

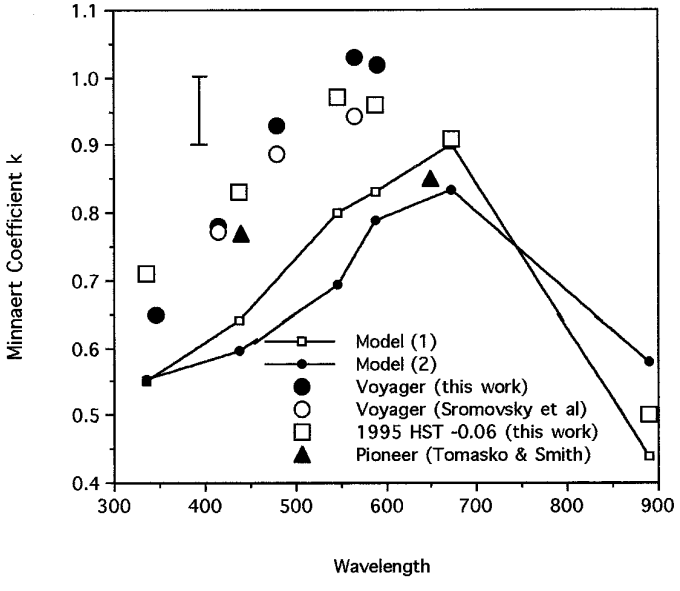

FIG. 4. Wavelength dependence of the Minnaert coefficient k. Squares show 1995 HST data, reduced by 0.06 to correct for the effects of the point-spread function, and filled circles are Voyager data. Reasonable agreement is found between HST and Voyager results (vertical bar shows our estimated error for both data sets). Our determinations seem consistent with the measurements by Sromovsky *et al.* (1981) for Voyager data (open circles) and Tomasko and Smith (1982) for Pioneer data (filled triangles). The lines correspond to the values for the "nominal" Lemmon (1994) model (model 1) of Titan, which reproduces the Neff *et al.* (1984) spectrum, and the same model with an extra 0.5 optical depths of haze added at 108 km (model 2).

we are at an extremum of the cycle. The best measurements for measuring the phase are during the zero-crossing, when the time derivative of the contrast is highest. We have made $1 + A\cos[(2\pi T/29.4)\text{-}\delta]$ fits (see Fig. 5), to the albedo ratio, with T the time in years, and A the amplitude of the contrast cycle. The amplitude A of the cycle (± 0.01) is 0.20 in blue and 0.15 in green, with a phase lag δ (computed from $T = 0$ at solstice in 1987.9—note that Saturn's orbit is eccentric, such that northern summer is longer than the winter) at both wavelengths of about 90°, with a probable error of ~10° (see also section 3.2). For this simple fit, we have used time as the independent variable, although equally L_s (the Titanocentric longitude of the sun), the solar latitude, or the true anomaly of Saturn's orbit could be used.

Although the difference is small, and comparable with the error bars, it may be seen in Fig. 3 that the contrasts seen by Voyager and Pioneer were slightly larger ($11 \pm 3\%$ at blue) than those we have measured for the present epoch ($9 \pm 2\%$), suggesting that the cycle may be somewhat asymmetric [contrast for a given NSA is given by the unsigned value of (NSA-1)/(NSA+1)]. Similarly, the fits in Fig. 5 in general lie inside the Voyager points but outside the HST points.

3.1. UV Asymmetry

Courtin (1992) and Courtin *et al.* (1991) reported observations and modeling of Titan's UV albedo and suggested that the NSA contrast should be greater in the UV (200–

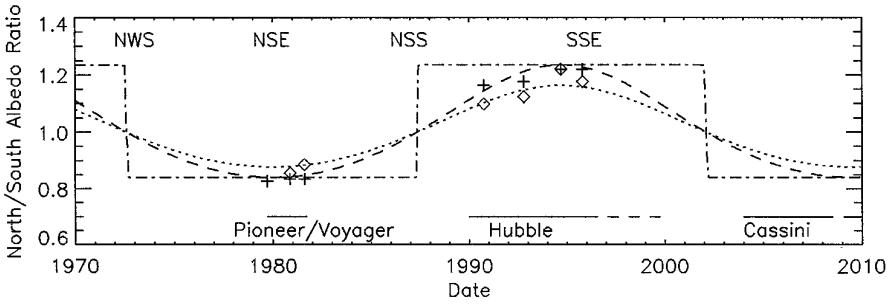

FIG. 5. Time evolution of the NSA at blue (F439W, crosses) and green (F547M, diamonds) wavelengths, together with sinusoidal fits (dashed and dotted lines, respectively). Error bars are comparable with symbol size. The dash–dot curve is a crude "square-wave" fit to the blue data. Abbreviations at top indicate approximate season (e.g., NWS, northern winter solstice; SSE, southern spring equinox, etc.).

260 nm) than in the visible. This suggestion was based on measured optical properties (Khare *et al.* 1984) of tholins and augmented by the condensation of organics. Figure 7 in Courtin (1992) suggests that the predicted NSA contrast at 260 nm should be ~15% greater than that in the blue, and at 200 nm, the contrast should be 40% greater. Toon *et al.* (1992) and Hutzell (1996) also predict strong UV contrasts.

This trend is not what is seen in either the Voyager or the HST data sets, which show that shorter than ~450 nm there is a consistent drop in NSA as wavelength decreases. Our observations in this spectral region are not ideal. One of the Saturn exposures used the F255W filter, and signal-to-noise is better than for the Voyager images, but poor compared with the other HST data. The motion of Titan on the (Saturn-tracking) image, together with the moderate exposure time, gives some smear. However, the measurement of the NSA is not significantly impeded by either of these drawbacks.

Additionally, we examined an image of Titan taken at ~230 nm with the Faint Object Camera. The signal-to-noise in this image was too poor to enable useful quantitative analysis, but qualitatively it could be seen that the asymmetry was far less than at blue wavelengths. All of the imaging data, then, argue against Courtin's (1992) suggestion that the UV asymmetry is stronger than at blue wavelengths.

The albedo of Titan at UV wavelengths is notoriously hard to model, as Rayleigh scattering from the atmosphere should tend to make it bright—see, for example, the models in Toon *et al.* (1992). To reduce the albedo to the observed low values requires small particles at high altitudes—perhaps the monomer particles that make up aggregate particles—to absorb the light. Aggregate particles (i.e., those formed by the clustering of smaller ones) typically exhibit the fractal nature of their properties, such as cross-sectional area, varying as a non-integral power of the number of monomer particles. Aggregate particles, often termed "fractal particles" or "fractal aerosols," exhibit the scattering phase function and polarization properties observed on Titan (West and Smith 1991, Lemmon, 1994). Fractal aerosols in Titan's atmosphere are also discussed in some detail by Rannou *et al.* (1995).

3.2. Comparison with Disk-Integrated Albedo

The available imaging data have rather poor temporal coverage to date, with information available only near the equinoxes of 1980 and 1995. Although no imaging data are available between 1981 and 1990, photometry of Titan has been obtained regularly since 1971 by Lockwood *et al.* (1986a,b, etc.) using yellow (551 nm) and blue (472 nm) filters. The relevant colors for HST comparison are the blue (F439W and F467M) and green (F547M) filters.

Figure 6 shows the normalized blue albedo of Titan from observations at Lowell observatory. The ~14-year periodical variation in albedo was first thought to be due to the solar cycle (Lockwood and Thompson 1979), with a similar period, but Sromovsky *et al.* (1981) showed that the variation can be reproduced if there is a varying contrast between Titan's hemispheres, with a peak contrast near equinox.

We fit a normalized north albedo A_N of the form $(1 + \Delta \sin \theta)$ and a south albedo A_S of $(1 - \Delta \sin \theta)$ and other analytic functions described and defined in Table III. The NSA is described by A_N/A_S, and the observed disk-integrated albedo is

$$A_O = cA_N + (1 - c)A_S, \tag{1}$$

where the north contribution c is the fraction of total light received from above the equator. This parameter c depends not only on Titan's orientation to the sun and earth, but also on the limb darkening, since stronger limb darkening enhances the contribution from those parts of Titan close to the center of the disk. From numerical experiments with synthetic images, making the simplifying assumption $\mu = \mu_0$, we find to within 1%,

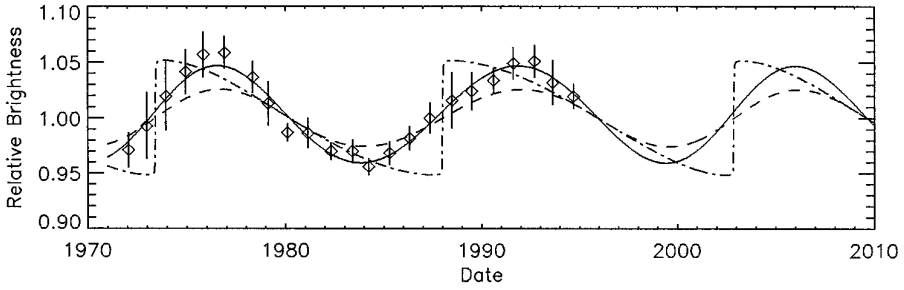

FIG. 6. Normalized blue albedo measurements of Titan taken at Lowell Observatory. Error bars are 3σ. The fitted curves are the "simple" analytic model 1 in Table III. Solid line, best fit to albedo data. The dashed line has amplitude for the best-fit to the NSA data (see Fig. 5). Dot–dash curve is the "square-wave" NSA (model 3), where contrast has constant amplitude but changes sign at solstice (see Fig. 5). The "modified" model (4) is indistinguishable from the solid line. The yellow albedo data look similar but is of lower amplitude and slightly phase shifted.

$$c = 0.5 + (0.0069 + 3.567 \times 10^{-3}k)\lambda, \qquad (2)$$

where k is the Minnaert coefficient described earlier, and λ is the latitude of the subsolar point in degrees. We assume Titan's equator lies in the ring plane.

We investigated albedo variations other than sinusoidal (e.g., a "square wave," wherein the NSA has a constant amplitude but reverses in sign around solstice) but the fit to the albedo curve is poor. This suggests that the asymmetry will decay smoothly from its present value. If a sinusoidal variation is assumed, but with an amplitude scaled by the normalized insolation, the fit is about as good as a simple sinusoid. We have also examined fits for the yellow albedo data recorded at Lowell and find similar results. Our best-fit results are summarized in Table II. Example fits to the blue albedo data are shown in Fig. 6.

TABLE III
Form and Quality of Fit for Various Analytic Models Used to Simultaneously Fit the Albedo and Contrast Data

Model	Parameters	RMS Error (Brightness)	RMS Error (NSA)	Comments
1.				
$A_N=(1+\Delta\sin(\theta))$, $A_S=(1-\Delta\sin(\theta))$	Δ=0.17 δ=-94°	0.0069•	0.163	Best simple fit to blue albedo
	Δ=0.16 δ=-94°	0.0070•	0.140	Demonstrates sensitivity to Δ
	Δ=0.17 δ=-90°	0.0084	0.156	Demonstrates sensitivity to δ
	Δ=0.13 δ=-102°	0.0071	0.124	Best simple fit to yellow albedo
	Δ=0.10 δ=-90°	0.0170	0.033•	Best simple fit to blue NSA
	Δ=0.07 δ=-92°	0.0158	0.025•	Best simple fit to yellow NSA
2.				
$A_N=(1+I\Delta\sin(\theta))$, $A_S=(1-I\Delta\sin(\theta))$	Δ=0.18 δ=-94°	0.0061•	0.173	Insolation-biased fit to blue albedo
	Δ=0.13 δ=-102°	0.0080•	0.112	Insolation-biased fit to yellow albedo
	Δ=0.10 δ=-94°	0.0144	0.031•	Insolation-biased fit to blue NSA
	Δ=0.07 δ=-92°	0.0154	0.027•	Insolation-biased fit to yellow NSA
3.				
$A_N=(1+\Delta Z)$, $A_S=(1-\Delta Z)$ $Z=[\text{sign}(\sin(\theta))]$	Δ=0.07 δ=-92°	0.0210	0.039•	Sample 'square-wave' NSA fit
4.				
$A_N=(1+\Delta\sin(\theta)+X\sin(2\theta))$	Δ=0.11 δ=-94°, X=0.015	0.0069•	0.043•	Best modified fit to blue
$A_S=(1-\Delta\sin(\theta)+X\sin(2\theta))$	Δ=0.08 δ=-100°, X=0.015	0.0062•	0.026•	Best modified fit to yellow

Note. RMS errors listed above should be compared with the estimated error in brightness ($1\sigma \sim 0.01$) and contrast (uncertainty ~ 0.03): acceptable fits indicated by •. It can be seen that while simple models can fit single data sets well, only a model in which there is an albedo enhancement (X) centered on times of peak NSA is able to simultaneously fit albedo and contrast data. In the model descriptions above, $\theta = (\Omega - \psi - \delta)$ where Ω is the true anomaly of Saturn (=0° at perihelion, 1974.0, $L_s = 279°$), ψ is the true anomaly at the equinox (261° at northern autumn equinox, 1995.9, $L_s = 180°$), δ measures the phase lag (the lag in the traditional sense is $180° - \delta$), and I is the relative insolation at Titan.

As noted by Smith *et al.* (1981), Sromovsky *et al.* (1981, 1986), and Lockwood *et al.* (1986b), the observed contrast between hemispheres is inadequate to reproduce the albedo variation. We also find this to be the case for the 1986–1995 epoch; i.e., a simple albedo function tuned to fit the NSA data is poor at reproducing the albedo and vice versa. The discrepancy between the cycle amplitude indicated by the imaging NSA measurements and that required to fit the albedo implies an effect additional to the asymmetry cycle. In analytic terms, the residual albedo variation (i.e., that part not reproduced by the asymmetry cycle) seems to be well reproduced with an increment to the albedo scaled to double the phase of the NSA (see model 4 in table III). The amplitude of this increment is about 50% larger than that of the seasonal asymmetry cycle. Lockwood *et al.* (1986b) suggest that physical possibilities are a solar cycle effect, that the change in insolation is due to Saturn's eccentricity, or a change in the location of the contrast boundary.

The solar cycle does not correlate well with the residual albedo variation (while it did so in the late 1970s, the solar cycle is now out of phase with the albedo variation), and in any case, as discussed below, the production of aerosols has such long time constant as to make it non-viable as a mechanism for generating albedo changes on seasonal timescales (see Hutzell 1993). Similarly, Saturn and Titan's insolation varies with Saturn's orbital period of 29.5 years, with a peak at perihelion in 1974 and a minimum in 1988. Since the residual albedo discrepancy has a period of about 14 years, it is difficult to relate it directly to the insolation variation.

Although the contrast boundary may indeed migrate north and south, we reject this mechanism as a principal cause of the discrepancy. If the albedo changed according to the simple (model 1 in Table III) law tuned to fit the NSA data, the contribution required from the brighter hemisphere would need to be greater than unity to reproduce the albedo variation. This is clearly unphysical. As the boundary between hemispheres is itself not very sharp, and is blurred by the psf in our HST images, it is not easy to measure. Smith *et al.* (1992) suggested a boundary at ~20°N. We find that the residuals after our model image subtraction are somewhat smaller with the interhemispheric boundary defined in the model at 10°N to 20°N, suggesting that the ''boundary'' lies in this range. Model images with boundaries south of the equator or north of 30°N are poor. This may be contrasted with Fig. 15 in Smith *et al.* (1982), which shows the transition region spanning about 30°S to 5°N. Squyres *et al.* (1984) report measuring the boundary at 5.5°S. Thus, while it appears that the boundary does appear to move, it moves in the wrong direction (i.e., on Titan, the darker ''hemisphere'' is the larger one) to account for the albedo variation.

A change in the global haze properties is a likely mechanism for the albedo variation. If the haze is described by altitude functions of particle size, number density, and optical properties, any or all of these could change at any or all altitudes. For convenience, however, we can think of the optical effects as changes in one or both of two parameters (one an input parameter, the assumed radius, and the other the limb darkening coefficient k) in our model images of Titan.

A change in radius of the ''optical surface'' could account for the additional ~2% of required brightness—increasing Titan's area by 2% implies an increase the altitude of the optical surface by 1%, or about 30 km, or one scale height. GCM results predict a general upwelling at low latitudes, where most of Titan's reflected light comes from, near equinox (see Hourdin *et al.* 1995) which could levitate most of the reflecting haze. Note that this refers to the normal optical depth=unity altitude near 100 km. Latitudinal variations in the altitude of the *tangential* optical limb (normal optical depth 0.01~0.03, at an altitude of 300 km or so) of order 50 km have been noted by Karkoschka and Lorenz (1997), Rages and Pollack (1983), and Hubbard *et al.* (1993). Model study is required to determine whether a physically plausible change in the optical surface would be accompanied by changes in reflectivity.

Physically the same process (a change in haze properties) could manifest itself in a change in the limb-darkening coefficient, with the ''radius'' held fixed. Numerical experiments show that for the same intrinsic reflectivity I_0, the disk-integrated brightness at zero phase varies as $\exp(-0.37k)$, with k the limb-darkening coefficient. Thus, a 2% increase in brightness would require a decrease in k of 0.05. The present analysis, however, is barely able to resolve such changes in k, and since there is not yet a set of imaging data using the same instrument with the same psf spanning more than a couple of years, confidence in detecting such a change would be poor.

4. MECHANISMS OF SEASONAL CHANGE: MODEL COMPARISON

We can use the wavelength dependence of the asymmetry, and its phase with respect to solar forcing, to investigate the physical processes causing the change. That the asymmetry has reversed over a period of 15 years is entirely consistent with it being due to solar forcing in one way or another, since Titan's substantial obliquity of 26.7° leads to strong interhemispheric variation in insolation with this period. Since the optical wavelengths under consideration are primarily sensitive to the atmospheric haze, this variation in albedo must be due to a change in the haze structure or optical properties in each hemisphere.

Sromovsky *et al.* (1981) considered aerosol parameters generated by Rages and Pollack (1980) and noted that

contrast would decrease or disappear for small phase angles if the contrast were due to a change in aerosol size. We, and Sromovsky *et al.* (1981), have found no evidence for such a drop in contrast at lower phase angles (based on analysis of Voyager images at phase angles from zero to 30°), so a size distribution change seems unlikely. Sromovsky and Fry (1989) measured the NSA out to phase angles of 90°, where a variation in mean size would give a contrast reversal, but found instead that the contrast was constant with phase.

Sromovsky *et al.* (1981) also considered whether a cloud layer deep in the atmosphere could cause the asymmetry. They argue that such a cloud layer would have to be more absorbing at short wavelengths to match Titan's geometric albedo (Rages and Pollack 1980), and thus the north–south contrast should be higher at long wavelengths, which is not what is observed, namely a decline and reversal of the asymmetry with increasing wavelength.

A change in aerosol absorption coefficient, due perhaps to condensation of materials onto the aerosols, is a possible mechanism, consistent with the blue and green asymmetry reported by Sromovsky *et al.* (1981). This mechanism is that favored by Courtin (1992) who noted a latitudinal correlation between the HCN to C_2H_4 atmospheric abundance ratio and albedo. A relevant observation is that by Letourneur and Coustenis (1993) who while reporting ''no significant temporal variations'' in a comparison of V2 IRIS data with that from V1, show estimates of the V2 abundance of C_4H_2 and C_3H_4 at high northern latitudes factors 3–5 lower than those estimated (Coustenis and Bézard 1995) for Voyager 1 at the same latitude. It is of note that these are the heaviest hydrocarbons they examined and thus are most likely to play a role in aerosol modification by condensation. However, condensation onto aerosols would amplify (Courtin 1992) the north–south contrast in the UV, which is clearly not what is observed. Thus while condensation may well occur, and may modify the aerosol optical properties, it is not the dominant effect. Toon *et al.* (1992) point out that one would not expect to see a reversal of contrast at long wavelengths if the cause of the asymmetry were a change in the optical properties of haze particles.

Having eliminated the mechanisms above as principal contributors, the remaining source of the contrast is additional aerosol opacity by an increase in the number density of particles. We will now investigate whether production, removal, or transport of aerosols is what controls their number density at the relevant altitudes.

We attempted to reproduce the contrast changes using a multi-layer radiative transfer model. This model (Lemmon 1994), using fractal aggregate particles, fits the spectrum of Titan measured by Neff *et al.* (1984) and Pioneer and Voyager polarimetry (Tomasko and Smith 1982). We find that the model qualitatively reproduces the wavelength dependence of the limb-darkening coefficients (Fig. 4) that we have determined for Titan. A change in model mass production rate (see Fig. 7) of a factor 2 generates the albedo difference fairly well, and it is of note that the Lemmon (1994) model, using fractal aggregate particles, performs much better at short wavelengths than the Toon *et al.* (1992) model which uses spheres. However, such a production change overestimates the contrast at near-IR wavelengths, probably by increasing the number density too much at high altitudes. We also considered the effect of changing the removal (''rainout'') altitude of the particles from 88 to 64 km. In effect this simply increases the number density of particles in this altitude range. Such a change (see Fig. 7) is unable to reproduce the contrast spectrum—light is scattered too high in the atmosphere for changes at ~70 km to generate enough blue contrast between these cases, although the near-IR contrast is reasonable.

Note that a drop in rainout altitude essentially increases aerosol opacity at the base of the haze layer, whereas a change in production rate drives the opacity at the top. We found (Smith *et al.* 1995) that the albedo difference with wavelength between north and south could be reproduced reasonably by introducing an ''artificial'' additional haze opacity, with particles bright in the red, dark in blue, with optical depth 0.5 in a 104–112 km altitude bin. Introducing such a layer has an effect broadly comparable with that of lowering the rainout altitude, although since the altitude is higher, the contrast in the methane band (889 nm) is rather stronger, as for the case where mass production was changed.

Figure 8 shows the altitude of the unity optical depth level in the nominal model, in very crude terms, large contrasts must be generated near or above these altitudes. Since the contrast is weaker at wavelengths below 400 nm, most of the contrast must be generated lower than ~120 km altitude. Models (e.g., where production rate is changed) where there are significant changes in the haze at higher altitudes tend to overpredict 889 nm contrasts. The cases above are single perturbations to a model haze structure—clearly what is actually happening on Titan is more complicated—some altitudes may be depleted in haze while others are enhanced. As pointed out by Hutzell (1996) contrast at different wavelengths may reflect changes in haze structure at different altitudes.

Note that we have deliberately not explored model variations in detail, as our nominal model—like that of Toon *et al.* (1992)—is tuned to fit the Neff *et al.* (1984) disk-integrated albedo data. A model tuned to fit this data may not, however, actually describe the haze strructure of any part of Titan, ever, since the albedo reflects the sum of (non-equal) contributions from two hemispheres. A future, more detailed model investigation will use the contribution factors described earlier and separate models for each hemisphere, tuned first to fit the Neff *et al.* (1984) data,

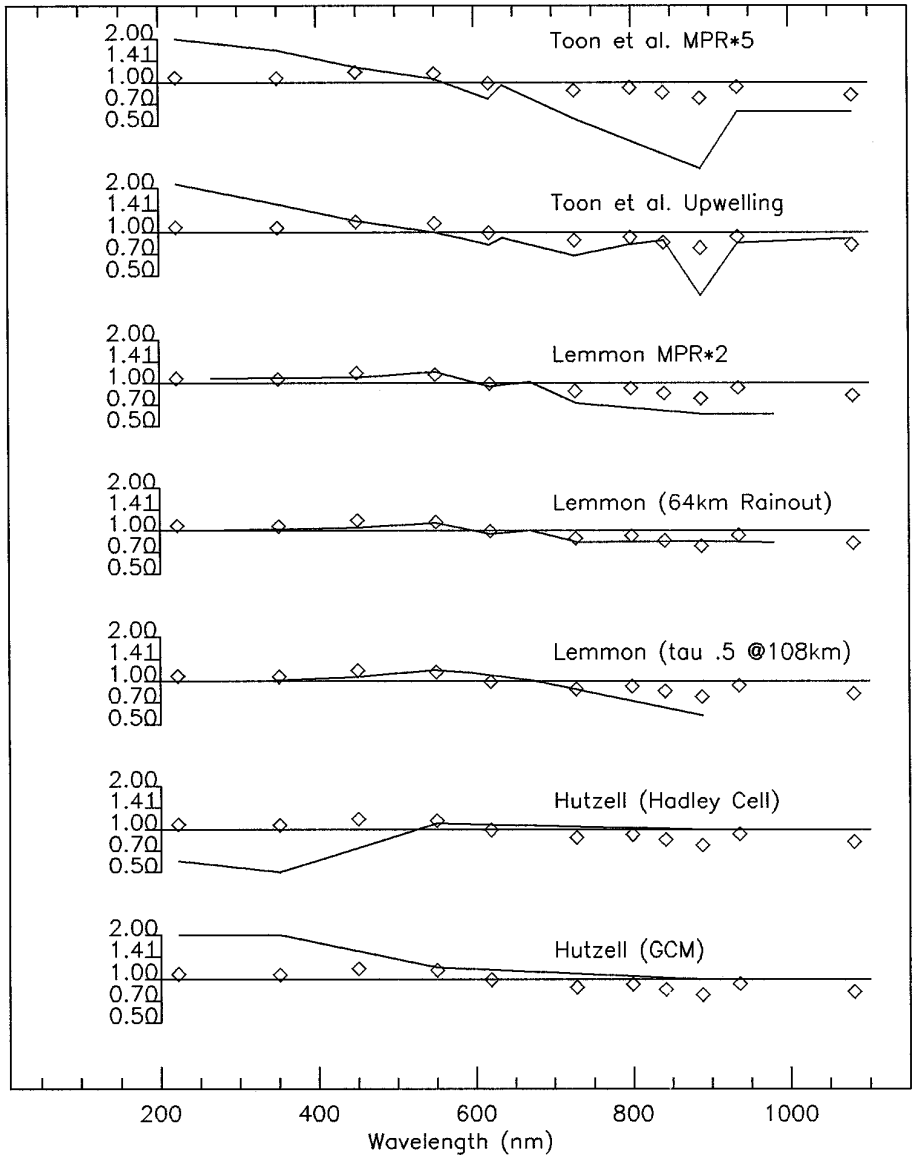

FIG. 7. Comparison of modeled albedo contrast (lines) due to various mechanisms with that observed by HST (diamonds). Plotted are ratios of model albedo tuned to fit Neff *et al.* (1984) spectrum divided by models with a 0.05 cm/sec updraft and factor 5 increase in aerosol mass production rate (MPR) from Figs. 9 and 13 of Toon *et al.* (1992) and for factor 2 increase in MPR and drop in rainout altitude from 88 to 64 km from Lemmon (1994) Figs. 23 and 24. The Lemmon model with an additional 0.5 optical depth of haze at 108 km are new calculations. The Hutzell data are north/south albedo ratios estimated from Hutzell *et al.* (1996) Fig. 5 for a global circulation model (GCM) and a Hadley-type circulation. The upwelling Toon and Lemmon rainout and 108 km cloud cases appear to perform best, although the Toon model does not perform well at short wavelengths.

and then each varied to reproduce the asymmetry cycle and albedo variation.

Limb-darkening coefficients can be estimated from the model and (see Fig. 4) are qualitatively in agreement with the observed values. The model does not take into account the combined depth and sphericity of the atmosphere into account, but these effects are only important at the limb, which represents perhaps 2 of the 10 points used to fit a k value. The model has not been tuned to fit the k values in any case. We note that the k values are sensitive to model parameters (see Fig. 4) so will be useful in constraining future models.

Direct production of aerosols by UV photolysis occurs at high altitude (>200 km), and we assumed, as Toon *et al.* (1992), that aerosols are removed by rainout. Although a change in steady-state aerosol mass production rate by a factor of 2 reproduces the contrast versus wavelength fairly well (see Fig. 7), Hutzell (1993) showed that the

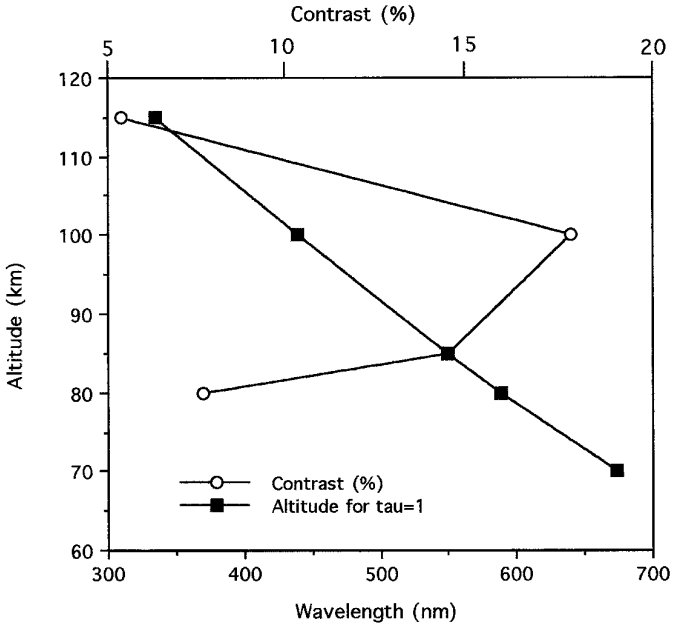

FIG. 8. Altitude of optical depth = 1 from Lemmon (1994) model as a function of wavelength (nm). Large contrasts must be generated at or above this level. If a measure of contrast is plotted on the abscissa, with the $\tau = 1$ altitude for the corresponding wavelength used as the ordinate, a lower limit for the altitude region responsible for the contrast is indicated.

amplitude and phase of the observed contrast for a variation in production rate on seasonal (~10 year) time scales is incompatible with observations. Essentially, the long residence time of haze particles is such that a change in production rate is damped out: the haze produced in one season contributes only a tiny fraction of the total column opacity.

Note also that while an increase of the rainout altitude from 64 to 88 km over a short period would clear that altitude range of aerosols, the terminal velocity of 0.1 to 1.0-μm spherical aerosols is such (Toon *et al.* 1992) that it would take between 10 and 80 years for descending aerosols to repopulate the layer after the rainout altitude had dropped again. This long time scale argues against this being a plausible mechanism for producing the contrast—the response time would tend to damp out the albedo difference, just as for production.

The Toon *et al.* (1992) upwelling model reproduces the blue and near-IR contrast (see Fig. 7), but is poor in the violet and UV and in the 889- and 619-nm methane bands: this may be due to poorly modeled methane absorption and/or the UV albedo problems already discussed, or both effects may be due in part to too high number density at high altitudes for the upwelling case. In reality, particles will be advected away at high altitudes rather than accumulate there: the streamlines turn over rather than stop. Upwelling in the present northern hemisphere is consistent with the detection in Titan's shadow of a detached haze layer in that hemisphere by Karkoschka and Lorenz (1996). Note that this detached haze layer is optically thin at normal incidence and does not significantly affect the albedo measurements reported here.

Hutzell *et al.* (1996) have investigated the effect of applying a Hadley cell type circulation, and the recent GCM results of Hourdin *et al.* (1995) to Titan's aerosols, but they use the Toon *et al.* (1992) optical scheme, which overestimates the contrast in the violet and UV. Hutzell *et al.* (1996, Fig. 5) show relative albedo as a function of latitude for when maximum contrast at 550 nm occurs: the predicted contrast for the GCM circulation is ~200% at 222 and 350 nm, far in excess of that observed. The contrast at 550 nm is broadly that which is observed, but at 889 nm, they predict high albedo at high latitudes, but no hemispheric asymmetry. As with the Toon *et al.* (1992) albedo calculations, the methane band and violet/UV treatments require revision. Hutzell's Hadley cell model appears to give a seasonal contrast of the wrong phase.

As the terminal velocity of particles 0.1 and 1 μm in radius is small (10^{-3}–10^{-2} cm/sec at 100 km altitude (Toon *et al.* 1992)), aerosol motion is coupled directly to the wind field. At that altitude (~10 mbar), the stream function of the zonally averaged meridonal flow (Hourdin *et al.* 1995) is 0.03 ~ 0.1 kg/sec, corresponding to velocities of ~1 m/sec. Thus, the transport of haze material from one hemisphere to the other takes only about 0.2 years. Thus a seasonal change in circulation seems the only plausible mechanism for introducing the additional haze opacity required on a sufficiently short time scales.

Our modeling and observations indicate that at equinox the autumn hemisphere (north at present, south during the Voyager encounter) is bright at visible wavelengths and that this is due to a lower haze opacity in the region of 100 km altitude. There is more haze in the spring hemisphere, which appears bright in methane band images. This is consistent with a pole-to-pole Hadley-type circulation which transports haze from the summer to winter hemispheres between equinoxes. The upwelling in the summer hemisphere also levitates some haze, with larger particles, providing the detached haze layer seen by Rages and Pollack (1983) and inferred by Karkoschka and Lorenz (1997).

Separating cause and effect in these seasonal changes is not easy. Temperature changes in the atmosphere could change the altitudes at which compounds might condense on aerosol particles, changing their size and/or optical properties. Courtin (1992) favors a change in optical properties of the haze particles as a mechanism for the asymmetry, especially in the UV. Recent work by Bézard *et al.* (1995) has shown that haze and gas opacity variations can account, radiatively, for at least part of the temperature asymmetry observed by Flasar *et al.* (1981). On the other

hand, the temperature asymmetry lag may simply be an artifact of the circulation: Flasar and Conrath (1990) suggested that the required phase lag in the observed temperature field could be due to deeper layers of the atmosphere being coupled to those levels where the asymmetry was observed (''dynamic inertia''). As Hutzell *et al.* (1996) point out, the situation is complicated, with the haze structure driving the energy deposition in the atmosphere and hence the circulation on which the haze structure depends. Further progress might be made by coupling a time-dependent haze model to a GCM.

We might expect that if the albedo contrast is circulation related, it may respond to changes in global insolation. Saturn's eccentric orbit provides such a modulation, such that insolation in 1974 was 20% higher than in 1989. We observe that the albedo contrast was slightly (indeed, within error bars, but at several wavelengths) smaller at present than at the Voyager epoch—if this change is real, and correlated with the insolation change, then we predict that the phase-corrected albedo ratio measured by Cassini will be closer to the Voyager values than those we have determined with HST. Note that we believe the effects of the solar UV cycle to be small, since the haze inventory can have only a small seasonally produced component.

5. ADDITIONAL DATASETS

Future monitoring by HST, using WFPC2, FOC, and after 1997 NICMOS, should allow the decay of the NSA to be studied. Additionally, progress in ground-based adaptive optics imaging of Titan has been impressive recently (Saint-Pe *et al.* 1993, Han *et al.* 1995, Combes *et al.* 1995). Although the emphasis on ground-based imaging has been on mapping surface features in the near-infrared (at 2 μm, where it is more practicable to compensate for atmospheric turbulence than at visible wavelengths), monitoring of the NSA should also be possible.

In the mid and far-infrared, the recently launched Infrared Space Observatory (ISO), although able to measure the abundances of a number of compounds in Titan's atmosphere (Coustenis *et al.* 1993), lacks the angular resolution to study the NSA. Its expected lifetime of 2 years may be enough to detect the seasonal variations in composition to which the NSA appears to be coupled, however.

During the 4-year (2004–2008) orbital tour of the Cassini mission, Titan's atmosphere will be extensively studied. Imaging from the UV to the mid-IR, as well as radio-occultations and far-infrared observations will provide a wealth of data, coupling optical appearance with wind and temperature fields and composition variations. Imaging observations will be of sufficient fidelity to measure the k variation over the 4-year period.

Despite the breadth and fidelity of anticipated spacecraft measurements, value of consistent, accurate ground-based monitoring of Titan's disk-integrated albedo over the years should also be noted: the combination of these data with the spatially resolved, but much more poorly sampled, imaging data has enabled the discrimination of different analytic models of Titan's behavior.

6. CONCLUSIONS

We have measured the north–south asymmetry in Titan's atmosphere from a number of HST images spanning the UV to the near-IR. The interhemispheric boundary, while blurred, is presently 10°–20° north of the equator, whereas it was about 5°S during the Voyager epoch. We find the NSA contrast peaks in the blue, falling off toward the UV. The NSA falls to near-zero at red wavelengths and reverses in the near-infrared due to methane absorption, and partly due to brightening of the aerosols. Of the wavelengths available on HST, the greatest contrast is found in the 889-nm methane band. These measurements are consistent with, but significantly extend the wavelength coverage of, earlier work by Smith *et al.* (1981), Sromovsky *et al.* (1981), Caldwell *et al.* (1992), and Smith *et al.* (1992, 1993).

The Minnaert coefficient follows a broadly similar pattern, with the strongest, near-Lambertian, limb darkening at green and red wavelengths. In the blue and UV, limb darkening is much weaker, with k tending toward 0.5, while in the near-IR methane band there is strong limb brightening (although the Minnaert fit is poor).

We find that the k values generated by a haze model reproduce the general wavelength dependence, although some discrepancies remain. Further, the k values are sensitive to model parameters, so our limb darkening measurements will be useful constraints on future models.

Existing haze models do not reproduce the wavelength variation of the asymmetry well. A change in number density in the 64–88 km altitude range (due, e.g., to a drop in rainout altitude), or at 108 km produce broadly correct near-IR contrasts, although a change in haze structure over a broader altitude range is likely what actually occurs—some change at higher altitudes is probably required to generate the blue contrast. Simply changing the mass production rate generates near-IR contrasts that are too high. As suggested by Toon *et al.* (1992) and Hutzell (1996), haze structure changes due to atmospheric circulation are a likely mechanism for the albedo contrast, although compositional changes (condensation) may also play a minor role.

We stress that present haze models, all tuned to fit the Neff *et al.* (1984) data set, may not represent the true haze structure of any part of Titan, since those albedo measurements are the weighted average of two hemispheres with clearly different haze structures. Future mod-

eling efforts need to consider models for (at least) two latitude ranges.

Our comparison of the variation of the disk-integrated albedo with a seasonally varying asymmetry suggests, as it did to earlier workers (Sromovsky *et al.* 1981, 1986, Lockwood *et al.* 1986b, etc.) that an additional global albedo variation is required—again a change in number density with altitude driven by circulation is a likely mechanism. The seasonal asymmetry appears to vary smoothly. Whether a smooth albedo variation necessarily implies a smooth variation of circulation is a question for future modeling.

At the time of writing, Titan's NSA has just passed its maximum intensity and will continue to decline (gradually, according to our albedo fits), and then reverse, over the next 15 years. During that time, we may continue to monitor it, with considerably better temporal and spatial resolution than the past 15 years.

ACKNOWLEDGMENTS

We thank Martin Tomasko for the use of the proposal 6030 images. RDL thanks Mary Guerrieri, Carolyn Porco, and Vance Haemmerle for assistance with retrieving and processing Voyager images. We also acknowledge the contributions of Steve Croft and Dhananjay Mahajan. Caitlin Griffith and an anonymous referee made comments which significantly improved the paper: we particularly acknowledge the diligent close attention of anonymous referee II who provided two sets of 10 single-spaced pages of comments. This work is based in part on observations with the NASA/ESA Space Telescope, and partial support was provided by NASA through Grant G0-5508.01-93A from the STScI, which is operated by AURA, Inc., under NASA Contract NAS 5-2655.

REFERENCES

Bézard, B., A. Coustenis, and C. P. McKay 1995. Titan's stratospheric temperature asymmetry: A radiative origin. *Icarus,* **113,** 267–276.

Burrows, C. J. (Ed.) 1995. *Wide Field and Planetary Camera 2 Instrument Handbook, STScI Publication.*

Caldwell, J. D., P. H. Smith, M. G. Tomasko, and H. Weaver 1992. Titan: evidence of seasonal change—A comparison of Voyager and Hubble Space Telescope images. *Icarus* **103,** 1–9.

Combes, M., L. Vapillon, E. Gendron, A. Coustenis, and O. Lai 1995. Spatially-resolved images of Titan in the near-infrared. *Bull Am. Astron. Soc.* **27,** 1106.

Courtin, R. 1992. *Titan's UV Albedo: Observations and Modeling,* pp. 59–67. ESA SP-338.

Courtin, R., R. Wagener, C. P. McKay, J. Caldwell, K.-R. Fricke, F. Raulin, and P. Bruston 1991. UV spectroscopy of Titan's atmosphere, planetary organic chemistry and prebiological synthesis. II. Interpretation of new IUE observations in the 220–335 nm range. *Icarus* **90,** 43–56.

Coustenis, A., and B. Bézard 1995. Titan's atmosphere from Voyager infrared observations. IV. Latitudinal variations of temperature and composition. *Icarus* **115,** 126–140.

Coustenis, A., Th. Encrenaz, G. Bjoraker, G. Graner, M. Ghang-Nhu, and E. Arie 1993. Modeling Titan's infrared spectrum for high-resolution spectral observations. *Icarus* **102,** 240–260.

Danielson, G. E., P. N. Kupferman, T. V. Johnson, and L. A. Soderblom 1981. Radiometric performance of the Voyager cameras. *J. Geophys. Res.* **86,** 8683–8689.

Flasar, F. M., and B. J. Conrath 1990. Titan's stratospheric temperatures: A case for dynamic inertia? *Icarus* **85,** 346–354.

Flasar, F. M., R. E. Samuelson, and B. J. Conrath 1981. Titan's atmosphere: Temperature and dynamics. *Nature* **292,** 693–698.

Han, B., T. Owen, A. Brahic, C. Dumas, F. Roddier, C. Roddier, M. Northcott, J. E. Graves, and D. O'Connor 1995. Ground-based near-infrared adaptive-optics imaging of the surface of Titan. *Bull. Am. Astron. Soc.* **27,** 1104.

Hourdin, F., O. Talagrand, R. Sadourny, R. Courtin, D. Gautier, and C. P. McKay 1995. Numerical simulation of the general circulation of the atmosphere of Titan. *Icarus* **117,** 358–374.

Hubbard, W. B., and 45 colleagues 1993. The occultation of 28 Sgr by Titan. *Astron. Astrophys.* **269,** 541–563.

Hunten, D. M., M. G. Tomasko, F. M. Flasar, R. E. Samuelson, D. F. Strobel, and D. J. Stevenson 1984. Titan. In *Saturn* (T. Gehrels and M. S. Matthews, eds.), pp. 671–759. Univ. Arizona Press, Tucson.

Hutzell, W. T., C. P. McKay, and O. B. Toon 1993. Effects of time-varying haze production on Titan's geometric albedo. *Icarus,* **105,** 162–174.

Hutzell, W. T., C. P. McKay, O. B. Toon, and F. Hourdin 1996. Simulations of Titan's brightness by a two-dimensional haze model. *Icarus* **119,** 112–129.

Karkoschka, E., and R. D. Lorenz 1997. Latitudinal variation of aerosol sizes inferred from Titan's shadow. *Icarus* **125,** 369–379.

Khare, B. N., C. Sagan, E. T. Arakawa, F. Suits, T. A. Callcott, and M. W. Williams 1984. Optical constants of organic tholins produced in a simulated Titanian atmosphere: From soft X-ray to microwave frequencies. *Icarus* **60,** 127–137.

Lane, A. L., C. W. Hord, R. A. West, L. W. Esposito, D. L. Coffeen, M. Sato, K. E. Simmons, R. B. Pomphrey, and R. B. Morris 1981. Photopolarimetry from Voyager 2: Preliminary results on Saturn, Titan and the Rings. *Science* **215,** 537–543.

Lara, L. M., R. D. Lorenz, and R. Rodrigo 1994. Liquids and solids on the surface of Titan: Results of a new photochemical model. *Planet. Space Sci.* **42,** 5–14.

Lemmon, M. T. 1994. *Properties of Titan's Haze and Surface.* Ph.D. Thesis, University of Arizona.

Letourneur, B., and A. Coustenis 1993. Titan's atmosphere from Voyager 2 infrared spectra. *Planet. Space Sci.* **41,** 593–602.

Lindal, G. F., G. E. Wood, H. B. Hotz, D. N. Sweetnam, V. R. Eshleman, and G. L. Tyler 1983. The atmosphere of Titan: An analysis of the Voyager 1 radio occultation measurements. *Icarus* **53,** 348–363.

Lockwood, G. W., and D. T. Thompson 1979. A relationship between solar activity and planetary albedos. Nature **280,** 43–45.

Lockwood, G. W., B. L. Lutz, D. T. Thompson, and E. S. Bus 1986a. The albedo of Titan. *Astrophys. J.* **303,** 511–530.

Lockwood, G. W., D. T. Thompson, and L. A. Sromovsky 1986b. Photometry of Titan: Evidence supporting the seasonal contrast model of albedo variations. *Bull. Am. Astron. Soc.* **18,** 809.

Neff, J. S., D. C. Humm, J. T. Bergstrahl, A. L. Cochran, W. C. Cochran, E. S. Barker, and R. G. Tull 1984. Absolute spectrophotometry of Titan, Uranus and Neptune: 3500–10500 A. *Icarus* **60,** 221–235.

Rages, K., and J. B. Pollack 1980. Titan aerosols—optical properties and vertical distribution. *Icarus* **41,** 119–130.

Rages, K., and J. B. Pollack 1983. Vertical distribution of scattering hazes in Titan's upper atmosphere. *Icarus* **55,** 50–62.

RANNOU, P., M. CABANE, E. CHASSEFIERE, R. BOTET, C. P. MCKAY, AND R. COURTIN 1995. Titan's geometric albedo: Role of the fractal structure of the aerosols. *Icarus* **118,** 355–372.

SAINT-PE, O., M. COMBES, F. RIGAUT, M. TOMASKO, AND M. FULCHIGNONI 1993. Demonstration of adaptive optics for resolved imagery of Solar System objects: Preliminary results on Pallas and Titan. *Icarus* **105,** 263–270.

SMITH, B. A., G. A. BRIGGS, G. E. DANIELSON, A. F. COOK II, M. E. DAVIES, G. E. HUNT, H. MASURSKY, L. A. SODERBLOM, T. C. OWEN, C. SAGAN, AND V. E. SUOMI 1977. Voyager imaging experiment. *Space Sci. Rev.* **21,** 103–127.

SMITH, B. A., L. A. SODERBLOM, R. BATSON, P. BRIDGES, J. INGE, H. MASURSKY, E. SHOEMAKER, R. BEEBE, J. BOYCE, G. BRIGGS, A. BUNKER, S. A. COLLINS, C. J. HANSEN, T. V. JOHNSON, J. L. MITCHELL, R. J. TERRILE, M. CARR, A. F. COOK II, J. CUZZI, J. B. POLLACK, G. E. DANIELSON, A. INGERSOLL, M. E. DAVIES, G. E. HUNT, D. MORRISON, T. OWEN, C. SAGAN, J. VEVERKA, R. STROM, AND V. SUOMI 1982. A new look at the Saturn system: The voyager 2 images. *Science* **215,** 504–537.

SMITH, B. A., L. A. SODERBLOM, R. BEEBE, J. BOYCE, G. BRIGGS, A. BUNKER, S. A. COLLINS, C. J. HANSEN, T. V. JOHNSON, J. L. MITCHELL, R. J. TERRILE, M. CARR, A. F. COOK II, J. CUZZI, J. B. POLLACK, G. E. DANIELSON, A. INGERSOLL, M. E. DAVIES, G. E. HUNT, H. MASURSKY, E. SHOEMAKER, D. MORRISON, T. OWEN, C. SAGAN, J. VEVERKA, R. STROM, AND V. SUOMI 1981. Encounter with Saturn: Voyager 1 imaging results. *Science* **212,** 163–182.

SMITH, P. H. 1980. The radius of Titan from pioneer Saturn data. *J. Geophys. Res.* **85,** 5943–5947.

SMITH, P. H., AND M. T. LEMMON 1993. HST images of Titan. *Bull. Am. Astron. Soc.* **25,** 1105. [Abstract]

SMITH, P. H., E. KARKOSCHKA, AND M. T. LEMMON 1992. Titan's north–south asymmetry from HST images. *Bull. Am. Astron. Soc.* **24,** 950. [Abstract]

SMITH, P. H., M. T. LEMMON, R. D. LORENZ, J. J. CALDWELL, M. D. ALLISON, AND L. A. SROMOVSKY 1996. Titan's surface, revealed by HST Imaging. *Icarus* **119,** 336–349.

SMITH, P. H., R. D. LORENZ, AND M. T. LEMMON 1995. New information on Titan's north–south contrast from HST. *Bull. Am. Astron. Soc.* **27,** 1104.

SQUYRES, S. W., W. R. THOMPSON, AND C. SAGAN 1984. Voyager imaging observations of Titan's atmosphere. 1. Disk-resolved photometric properties. *Bull. Am. Astron. Soc.* **16,** 664.

SROMOVSKY, L. A., AND P. M. FRY 1989. The phase variation of Titan's brightness contrast: Implied constraints on properties of haze particles. *Bull. Am. Astron. Soc.* **21,** 959.

SROMOVSKY, L. A., G. W. LOCKWOOD AND D. T. THOMPSON 1986. Titan's albedo variation: Relative influence of solar UV and seasonal contrast mechanisms. *Bull. Am. Astron. Soc.* **18,** 809.

SROMOVSKY, L. A., V. E. SUOMI, J. B. POLLACK, R. J. KRAUS, S. S. LIMAYE, T. OWEN, H. E. REVERCOMB, AND C. SAGAN 1981. Implications of Titan's north–south brightness asymmetry. *Nature* **292,** 698–702.

TOMASKO, M. G., AND P. H. SMITH 1982. Photometry and polarimetry of Titan: Pioneer 11 observations and their implications for aerosol properties. *Icarus* **51,** 65–92.

TOON, O. B., C. P. MCKAY, C. A. GRIFFITH, AND R. P. TURCO 1992. A physical model of Titan's aerosols. *Icarus* **95,** 24–53.

WEST, R. A., AND P. H. SMITH, 1991. Evidence for aggregate particles in the atmospheres of Titan and Jupiter. *Icarus* **90,** 330–333.